IOPscience iopscience.iop.org

Home Search Collections Journals About Contact us My IOPscience

Overview of L–H power threshold studies in NSTX

This article has been downloaded from IOPscience. Please scroll down to see the full text article.

2010 Nucl. Fusion 50 064010

(http://iopscience.iop.org/0029-5515/50/6/064010)

View the table of contents for this issue, or go to the journal homepage for more

Download details:
IP Address: 198.35.3.144
The article was downloaded on 03/01/2011 at 20:41

Please note that terms and conditions apply.

IOP PUBLISHING and INTERNATIONAL ATOMIC ENERGY AGENCY NUCLEAR FUSION
Nucl. Fusion **50** (2010) 064010 (8pp) doi:10.1088/0029-5515/50/6/064010

Overview of L–H power threshold studies in NSTX

R. Maingi[1], S.M. Kaye[2], R.E. Bell[2], T.M. Biewer[1], C.S. Chang[3], D.A. Gates[2], S.P. Gerhardt[2], J. Hosea[2], B.P. LeBlanc[2], H. Meyer[4], D. Mueller[2], G-Y. Park[3], R. Raman[5], S.A. Sabbagh[6], T.A. Stevenson[2] and J.R. Wilson[2]

[1] Oak Ridge National Laboratory, Oak Ridge, TN 37831, USA
[2] Princeton Plasma Physics Laboratory, PO Box 451, Princeton, NJ 08543, USA
[3] New York University, New York, NY, USA
[4] UKAEA Fusion, Culham, UK
[5] University of Washington, Seattle, WA, USA
[6] Columbia University, New York, NY, USA

Received 23 October 2009, accepted for publication 15 March 2010
Published 28 May 2010
Online at stacks.iop.org/NF/50/064010

Abstract
A summary of results from recent L–H power threshold ($P_{\rm LH}$) experiments in the National Spherical Torus Experiment is presented. First $P_{\rm LH}$ (normalized linearly by plasma density) was found to be a minimum in double-null configuration, tending to increase as the plasma was shifted more strongly towards lower- or upper-single null configuration with either neutral beam or rf heating. The measured $P_{\rm LH}/n_{\rm e}$ was comparable with neutral beam or rf heating, suggesting that rotation was not playing a dominant role in setting the value of $P_{\rm LH}$. The role of triangularity ($\delta_{\rm bot}$) in setting $P_{\rm LH}/n_{\rm e}$ is less clear: while 50% less auxiliary heating power was required to access H-mode at low $\delta_{\rm bot}$ than at high $\delta_{\rm bot}$, the high $\delta_{\rm bot}$ discharges had lower ohmic heating and higher $\mathrm{d}W/\mathrm{d}t$, leading to comparable loss of power over a range of $\delta_{\rm bot}$. In addition, the dependences of $P_{\rm LH}$ on the density, species (helium versus deuterium), plasma current, applied non-axisymmetric error fields and lithium wall conditioning are summarized.

PACS numbers: 52.55.Fa, 52.40.Hf

(Some figures in this article are in colour only in the electronic version)

1. Introduction

Ever since its discovery [1], the high-confinement mode or 'H-mode' has been the preferred operational scenario for many fusion research devices, and is the projected baseline operational scenario for the ITER [2]. The density and temperature profiles both broaden in the H-mode, leading to a reduced plasma pressure peaking factor which has been shown to allow higher stored energy limits [3, 4]. In addition, the extra pressure gradient at the edge drives a substantial bootstrap current, reducing the need for current drive. While these last two points are advantages, it should be noted that strong pressure gradient in H-mode usually drives edge localized modes (ELMs), which are predicted to lead to unacceptable erosion of plasma facing components in future devices, such as the ITER, unless the magnitude of the transient wall loadings can be maintained at a very low level.

Access to the H-mode is typically observed when the auxiliary heating power ($P_{\rm aux}$) crosses a critical value, leading to a bifurcation in the edge plasma profiles and a substantial reduction in the measured plasma turbulence. While the trigger for the L–H transition has remained elusive, the minimum level of heating for H-mode access (the L–H power threshold, $P_{\rm LH}$) has been compared across devices, with the main parametric dependences measured as $P_{\rm LH}[\mathrm{MW}] = 0.0488 n_{\rm e20}^{0.72} B_{\rm t}^{0.80} S_{\rm A}^{0.94}$, where $n_{\rm e20}$ is the plasma line-average density ($10^{20}\,\mathrm{m}^{-3}$), $B_{\rm t}$ is the vacuum toroidal field at the magnetic-axis (T) and $S_{\rm A}$ is the plasma boundary surface area (m^2) [5]. An alternate expression that may be more appropriate for comparison of different aspect ratio devices is given by $P_{\rm LH} = 2.15 n_{\rm e20}^{0.78} B_{\rm t}^{0.77} a^{0.98} R^{1.0}$, where a and R are the minor and major radii (m) [5].

However, it is known that each device has other dependences of $P_{\rm LH}$, which are collectively lumped into the nomenclature of 'hidden variables'. These include variations of the plasma boundary shape (number of X-points and magnetic balance, radial/poloidal/vertical location of X-points and plasma elongation) as well as the effect of plasma species, the effect of applied 3D non-axisymmetric fields and other parameters even more difficult to quantify, e.g. wall

 © 2010 IAEA, Vienna Printed in the UK & the USA

conditioning techniques or the effect of neutrals. The dependences of P_{LH} on these hidden parameters are receiving renewed interest because of the anticipated heating power availability in ITER, and the desire to access the H-mode early in ITER operation prior to the high activation phase with deuterium and tritium, i.e. in a hydrogen or helium campaign [6]. An additional consideration is the ITER plan for suppression of ELMs with 3D resonant magnetic perturbations, and whether such perturbations affect the P_{LH} value [6]. Motivated partly by the ITER requests and also by the need for projection of P_{LH} for future spherical tori designs, a broad range of experiments directed mainly at the 'hidden variables' has been conducted in the National Spherical Torus Experiment (NSTX) [7], with the first set of results documented in the remainder of this paper.

2. Normalization of the power threshold with plasma density

In general, H-mode access is routine in NSTX, typically enabled by auxiliary heating from neutral beam injection (NBI, P_{NBI}) or from radio frequency (P_{rf}) heating. Under some conditions, ohmic H-mode is also observed [8]. Measurement of the P_{LH} can be accomplished with either of the auxiliary heating techniques. The global results from a group of very recent LH power threshold experiments are summarized in this section, with details to be provided in a paper at the 2010 IAEA Fusion Energy Conference.

We first discuss the dependence of P_{LH} on line-average density ($\overline{n_e}$), to clarify the appropriate density normalization for the rest of this paper. Specifically we find $P_{LH} \sim \bar{n}_e^{\alpha}$, where $0.8 < \alpha < 1.2$ as long as low density locked modes are avoided. Note that a minimum density for accessing H-modes is typically set by the occurrence of low density locked modes (in the range of $1.5 \times 10^{19}\,\mathrm{m}^{-3}$ at plasma current $I_p = 0.65$ MA and increasing with I_p). The results presented in this paper were above that locked mode minimum density, and P_{LH} was normalized linearly by $\overline{n_e}$, i.e. using $\alpha = 1$. We note that normalization using $\alpha = 0.72$ or $\alpha = 0.78$ from the international P_{LH} scalings in section 1 does not substantially alter the results.

The dependence of P_{LH} on main ion species was measured in deuterium and helium discharges. This measurement was facilitated by slow ramps of the rf power, which allow for easier localization of the value of P_{LH} because the L–H transition occurs within ~10 ms of exceeding the threshold power. Note that the measured rf heating efficiency is comparable for helium and deuterium at the applied wave number $k_\parallel \sim 8\,\mathrm{m}^{-1}$. First, we note that the $\overline{n_e}$ in the helium discharges was somewhat higher than the deuterium discharges. When normalized by the $\overline{n_e}$ from Thomson scattering, the P_{LH} was comparable between deuterium and helium discharges, in agreement with results reported by the ASDEX-Upgrade device [9]. Note that these discharges were all above the low density threshold for locked modes.

A strong increase in $P_{LH}/\overline{n_e}$ with increasing plasma current (I_p) was measured, confirming earlier preliminary studies [10]. The previous results were complicated by the presence of locked modes at the very highest value of I_p. Here, the locked modes were avoided through improved discharge programming, and the P_{LH} was measured with P_{NBI} steps. Specifically $P_{LH}/\overline{n_e}$ increased from 0.7 to $1.2\,\mathrm{MW}/10^{19}\,\mathrm{m}^{-3}$ when I_p was increased from 0.7 to 1.0 MA, i.e. the measured dependence was faster than linear.

A strong increase in $P_{LH}/\overline{n_e}$ with applied 3D fields was also measured. An $n = 3$ field of 500 A coil current was applied with a set of six midplane window-frame coils external but close-fitting to the vacuum vessel [11, 12]. The resulting radial field perturbation ΔB_r was 10 G at the separatrix, with a $\Delta B_r/|B| \sim 3.3 \times 10^{-3}$. The $n = 3$ field was ramped up during the I_p ramp, thereby increasing $P_{LH}/\overline{n_e}$ from 0.65 to $1.0\,\mathrm{MW}/10^{19}\,\mathrm{m}^{-3}$. The effect of the $n = 3$ field at the time of the L–H transition was subtle, suggesting that the increase in P_{LH} was a 3D effect and not the result of a drastic change in the toroidal rotation profile.

Finally a ~33% decrease in $P_{LH}/\overline{n_e}$ was measured with the use of lithium wall conditioning. Lithium is evaporated via a set of overhead *in situ* lithium ovens in NSTX; shutters are used to prevent evaporation during the discharges [13]. For these experiments the total evaporation between discharges was ~200 mg, obviating the need for helium glow discharge cleaning between discharges. On the other hand, the reference unconditioned discharges used ~11 min of helium glow discharge cleaning between discharges to remove the embedded deuterium from the previous discharge. The recycling in discharges with lithium coatings was greatly reduced, with an ~80% drop in the divertor D_α emission. Consequently the $\overline{n_e}$ was indeed much lower in the lithium discharges, as expected.

3. Role of magnetic balance

3.1. Neutral beam heating

In this section, the dependence of P_{LH} on the magnetic balance is documented. Separate sets of control coils in the lower and upper regions of the NSTX allow flexible control over the X-point locations. The control parameter (δ_r^{sep}) used here is the radial separation between the upper and lower X-points, mapped to the outer midplane with a standard EFIT equilibrium [14, 15]. By convention $\delta_r^{sep} > 0\ (< 0)$ signifies that the upper (lower) X-point is closer to the plasma and hence dominant. A value of $\delta_r^{sep} = 0$ signifies a perfectly balanced double-null (DN), although a $|\delta_r^{sep}|$ value less than a poloidal ion gyro-radius (typically 4–8 mm for the NSTX outer midplane) is effectively balanced. Previously it was shown that the P_{LH} was a minimum at or very near DN configuration in both the MAST and the ASDEX-Upgrade devices [16, 17]. In contrast, the P_{LH} was a minimum in lower-single null (LSN) discharges with favourable ion ∇B drift in Alcator C-Mod [18], although its small poloidal ion gyro-radius may prevent the achievement and diagnostic confirmation of a pure DN in that device.

The achieved δ_r^{sep} variation of the NSTX discharges with P_{heat} closest to P_{LH} is shown in figure 1(*a*). In essence, this experiment is a comparison of the power threshold in DN, LSN (favourable ion ∇B drift) and upper single-null (USN, unfavourable ion ∇B drift) boundary shapes. As a result of the programmed variation in δ_r^{sep}, the elongation κ is indeed different between the three discharges, with $\kappa \sim 1.7$–1.8 in the LSN and USN discharges and $\kappa \sim 2$ in the DN discharge.

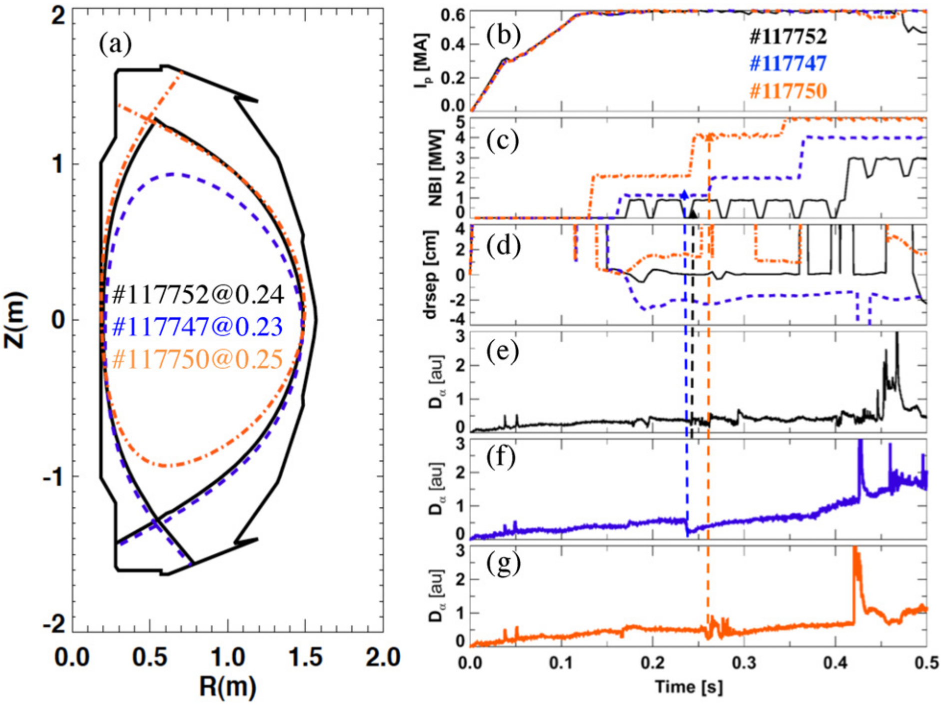

Figure 1. Discharges in δ_r^{sep} scan with NBI: (*a*) three shapes showing DN, LSN and USN discharges. The temporal evolution of these discharges is shown: (*b*) I_p, (*c*) NBI power, (*d*) δ_r^{sep}, (*e*)–(*g*) divertor D_α emission for each of the three discharges. The L–H transition times are indicated with arrows.

The other relevant discharge parameters are plasma current $I_p = 0.6$ MA, toroidal field on-axis $B_t = 0.45$ T, safety factor $q_{95} \sim 8$ and lower divertor triangularity $\delta_{bot} \sim 0.5$. The line-average density at the time of the L–H transition varied between 1.8 and $2.2 \times 10^{19}\,m^{-3}$. Note that certain elements of this study were previously described [19]; the full analysis of heating power and loss power at the L–H threshold has since been completed and is presented here.

The time evolution of the discharges with P_{heat} just above P_{LH} is shown in figures 1(*b*)–(*g*). The P_{NBI} was increased in steps through beam voltage variations and pulse-width modulation for the DN discharge (figure 1(*c*)). Arrows indicate the time of the L–H transitions on the divertor D_α traces in figures 1(*e*)–(*g*). It can be seen that the DN discharge required (figure 3(*e*)) the lowest P_{NBI} of 0.6 MW to trigger the H-mode (actually 0.9 MW with 67% pulse-width modulation), followed by the LSN discharge (figure 3(*f*)) with P_{NBI} of 1.1 MW and the USN discharge (figure 3(*g*)) with P_{NBI} of 4.0 MW.

Figure 2 displays various measures of the exhaust power as a function of δ_r^{sep}, with discharges with P_{NBI} closest to P_{LH} indicated with circles. Typically the power flow through the separatrix (P_{loss}) is computed just prior to the L–H transition:

$$P_{loss} = P_{heat}^{net} + P_{OH} - dW_p/dt, \quad (1)$$

$$P_{heat}^{net} = P_{aux} \times f_{abs} \times \left(1 - f_{loss}^{fast\ ion}\right) \times \left(1 - f_{loss}^{CX}\right) - P_{rad}, \quad (2)$$

where P_{heat}^{net} is the net heating power, P_{OH} is the ohmic heating power, dW_p/dt is the time derivative of the total plasma stored energy, P_{rad} is the core radiated power, P_{aux} is the auxiliary heating power, f_{abs} is the fraction absorbed by the plasma, $f_{loss}^{fast\ ion}$ is the fast ion loss fraction (for neutral beams) and f_{loss}^{CX} is the fraction lost due to charge exchange. The various fractions in equation (2) are computed with the TRANSP code [20]. The quantities P_{heat}^{net} and P_{OH} are available directly through the EFIT equilibrium reconstruction, or also through the TRANSP calculation, which includes the role of the effective average charge number Z_{eff}. The intent in showing the multiple panels is to highlight the effect of the various components in equation (1), in particular because inclusion of all the terms alters the ordering of the P_{LH} values, as compared with the raw auxiliary heating power levels needed to access H-mode. This is particularly important for the data in section 4.

Figure 2(*a*) shows P_{heat}^{net} values from the discharges in the study, with the heating powers closest to the P_{LH} indicated with ovals. The DN discharges with $\delta_r^{sep} \sim 0$ clearly have the lowest required P_{heat}^{net} for an L–H transition, consistent with the observed trend in P_{NBI} shown in figure 1. Figure 2(*b*) shows that the P_{heat}^{net} normalized by $\overline{n_e}$ still shows a clear reduction in the DN configuration, although the difference between DN and LSN is not as substantial as in figure 2(*a*). This normalization is relevant because of the observed dependence of P_{LH} on $\overline{n_e}$ discussed in section 2. Figure 2(*c*) shows that the trend of lowest P_{LH} in DN is still observed using the sum of the P_{heat}^{net} and P_{OH} (normalized by $\overline{n_e}$). Finally the full P_{loss} from equation (1) (normalized by $\overline{n_e}$) is shown in figure 2(*d*). Here the difference between DN and LSN is no longer outside the statistical error bars, as the DN discharges tended to have lower dW_p/dt than the other discharges. The error bars also increased, because the difference between the TRANSP and EFIT calculations was substantial in some cases. Further clarification requires additional experiments in which the L–H transitions are triggered at times of relatively constant P_{OH} and low dW_p/dt. As a point of reference, we note that the measured minimum P_{LH} was 5–6 times the values predicted by the multi-machine scalings discussed in section 1 [5].

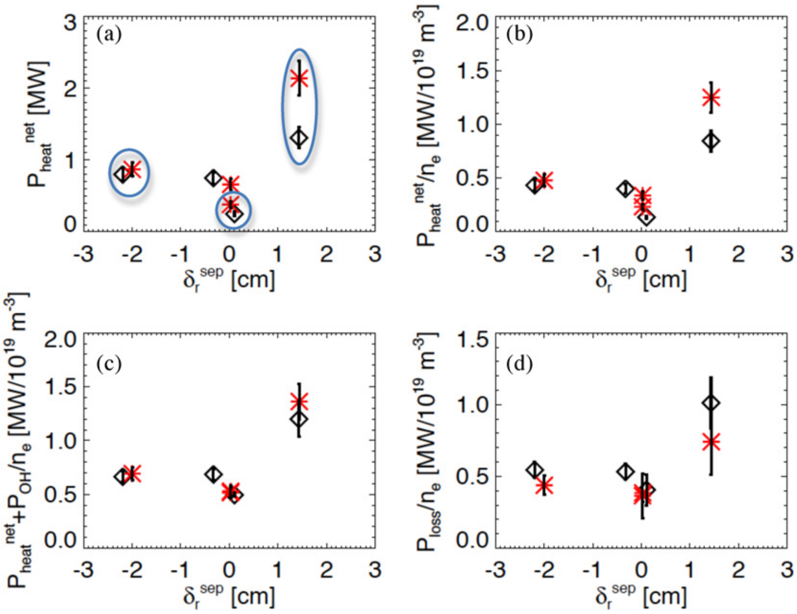

Figure 2. Various metrics of input power as a function of δ_r^{sep} with NBI heating: (*a*) P_{heat}^{net}, (*b*) P_{heat}^{net} normalized by $\overline{n_e}$, (*c*) (P_{heat}^{net} + P_{oh}) normalized by $\overline{n_e}$ and (*d*) P_{loss} normalized by $\overline{n_e}$. The red stars represent data just prior to an L–H transition and the black diamonds represent data that did not have an L–H transition. Ovals mark discharges closest to the power threshold.

3.2. Rf heating

Insight into the important factors affecting the L–H transition can be obtained by comparing transitions triggered with rf heating to the ones with neutral beam heating. Rf heating allows a separation of heat input from momentum and particle input, thereby differentiating it from neutral beam heating in which all three are normally coupled. In addition nearly all of the rf power is absorbed by the electrons, whereas the NBI power is split between the electrons and ions, typically with a 2 : 1 ratio. In the NSTX, rf heating is provided with the high harmonic fast wave (HHFW) system, with available power to the plasma up to 6 MW [21, 22]. While many antenna phasings are possible, these experiments were conducted with $k_\parallel \sim 14\,\mathrm{m}^{-1}$ (symmetric 0–π–0–π phasing) that provides the highest heating efficiency.

A DN boundary shape similar to the one in figure 1(*a*) was chosen as the baseline, with the outer gap reduced from 10 to 3 cm for optimal rf coupling. The other relevant discharge parameters were identical to the NBI experiment in section 3.1: $I_p = 0.6$ MA, $B_t = 0.45$ T, $q_{95} \sim 8$ and $\delta_{bot} \sim 0.5$. The δ_r^{sep} variation achieved with rf heating to localize the power threshold is shown in figure 3(*a*); note that data from more shapes between DN and LSN were obtained in this scan than for the NBI portion in 3.1.

The time evolution of the discharges with P_{heat}^{net} just above P_{LH} is shown in figures 3(*b*)–(*g*). The P_{rf} was increased in ~80 ms steps (figure 3(*c*)). Arrows indicate the time of the L–H transitions on the divertor D_α traces in figures 3(*e*)–(*g*). It can be seen that the DN discharge (figure 3(*e*)) required the lowest P_{NBI} of 1.1 MW to trigger an L–H transition, followed by the near-DN discharge ($\delta_r^{sep} \sim -0.6$ cm, figure 3(*f*)) with P_{NBI} of 1.7 MW and the LSN discharge ($\delta_r^{sep} \sim -1.8$ cm, figure 3(*g*)) with P_{NBI} of 2.8 MW. Discharges with $\delta_r^{sep} < -2$ cm or with $\delta_r^{sep} > 0.3$ cm failed to produce L–H transitions at the highest rf heating power.

The analysis to convert from P_{aux} to P_{loss} differs slightly from the method described in section 3.1. Specifically $f_{abs} = 0.8 \pm 25\%$ was obtained from the transient response of the plasma stored energy to rf power steps and both $f_{loss}^{fast\ ion}$ and f_{loss}^{CX} are neglected. Finally the P_{OH} and dW_p/dt values are obtained from the EFIT equilibrium reconstruction, as opposed to an arithmetic average of the TRANSP and EFIT analysis.

Figure 4 shows the same measures of input power versus δ_r^{sep} as discussed above for figure 2, with the heating powers closest to the P_{LH} indicated with ovals in figure 4(*a*). In this case, the trend that the DN discharge with $\delta_r^{sep} \sim 0$ had the lowest L–H transition power is maintained in all plots. Inclusion of the P_{OH} and dW_p/dt terms for P_{loss} does reduce the magnitude of the trend, re-emphasizing the need for additional experiments in which the L–H transitions are triggered at times of relatively constant P_{OH} and low dW_p/dt. One additional point: the $P_{loss}/\overline{n_e}$ at the L–H transition is ~40% higher for rf heating than NBI heating, but with overlapping error bars. Additional experiments are needed to determine whether the smaller outer gap required for the rf heating played a role. As previously reported [20], the rotation profiles differed considerably between the rf and NBI discharges. Taken in conjunction with the non-axisymmetric field application results discussed in section 2, the precise role of rotation in setting the value of P_{LH} remains unclear, i.e. in apparent contrast to the DIII-D results demonstrating a strong effect of rotation on P_{LH} [28]. As a point of reference, we note that the measured minimum P_{LH} was four times the values predicted by either of the multi-machine scalings discussed in section 1 [5].

4. Role of lower divertor triangularity

The triangularity of the dominant divertor has been shown to affect the stability limit of the H-mode pedestal, i.e. the point at which the pressure gradient and/or edge current exceed

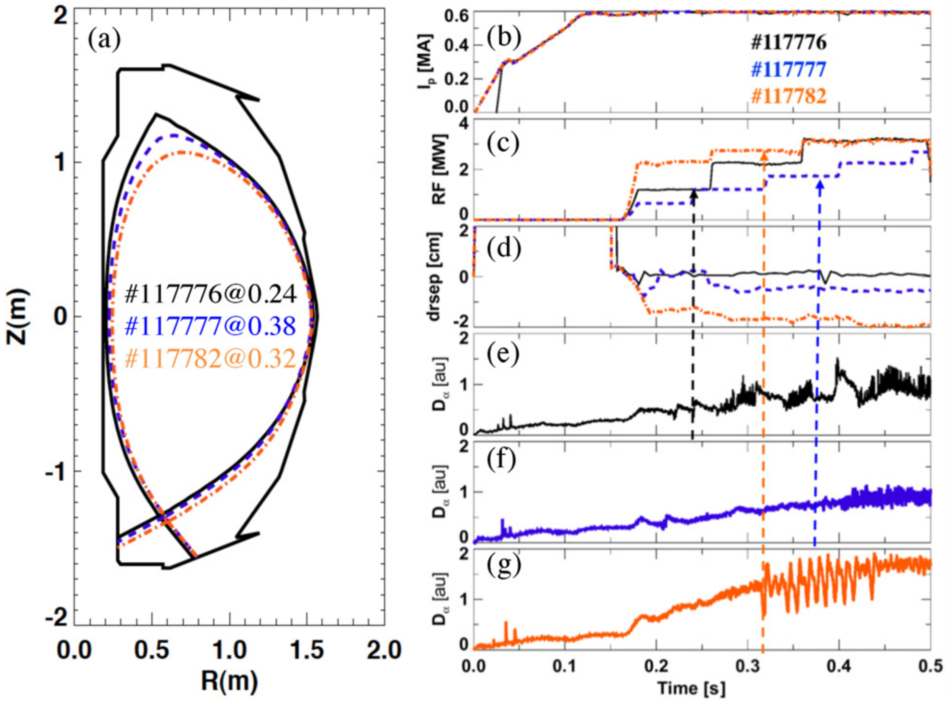

Figure 3. Discharges in $\delta_r^{\rm sep}$ scan with rf: (*a*) three shapes showing DN, marginal LSN and strong LSN discharges. The temporal evolution of these discharges is shown: (*b*) $I_{\rm p}$, (*c*) NBI power, (*d*) $\delta_r^{\rm sep}$, (*e*)–(*g*) divertor D_α emission for each of the three discharges. The L–H transition times are indicated with arrows.

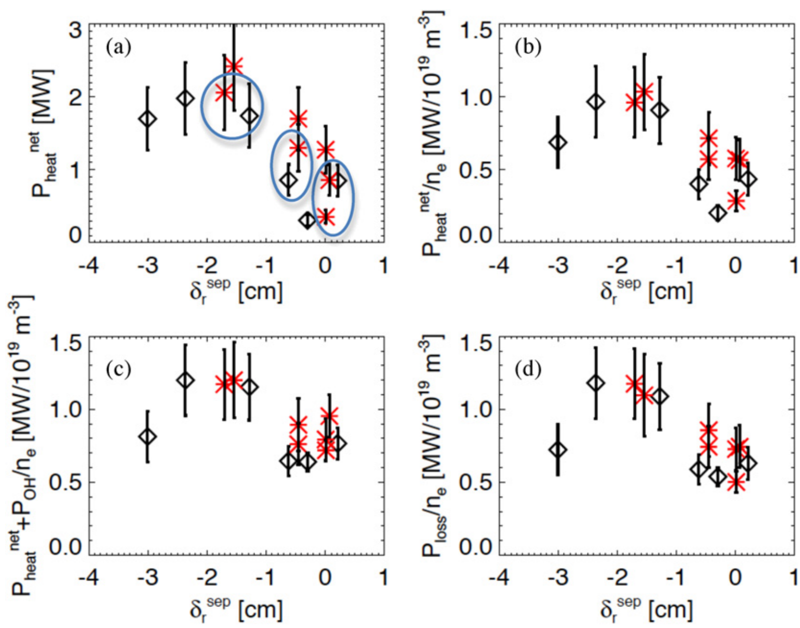

Figure 4. Various metrics of input power as a function of $\delta_r^{\rm sep}$ with rf heating: (*a*) $P_{\rm heat}^{\rm net}$, (*b*) $P_{\rm heat}^{\rm net}$ normalized by $\overline{n_{\rm e}}$, (*c*) ($P_{\rm heat}^{\rm net}$ + $P_{\rm oh}$) normalized by $\overline{n_{\rm e}}$ and (*d*) $P_{\rm loss}$ normalized by $\overline{n_{\rm e}}$. The red stars represent data just prior to an L–H transition and the black diamonds represent data that did not have an L–H transition. Ovals mark discharges closest to the power threshold.

critical values and trigger magnetohydrodynamic instabilities thought to be responsible for ELMs [23–25]. In this section, we document the dependence of power threshold on the lower divertor triangularity. This experiment was motivated in part by calculations with the XGC-0 neoclassical transport code [26] that showed increasing orbit loss of thermal ions with increasing X-point radius, i.e. decreasing $\delta_{\rm bot}$. As a result, larger radial electric field, E_r, and shear, E_r', were predicted with decreasing $\delta_{\rm bot}$. Anticipating that a critical E_r or E_r' might be needed to trigger an L–H transition, it follows that discharges with small $\delta_{\rm bot}$ would have a lower L–H power threshold than discharges with a higher $\delta_{\rm bot}$. Care must be

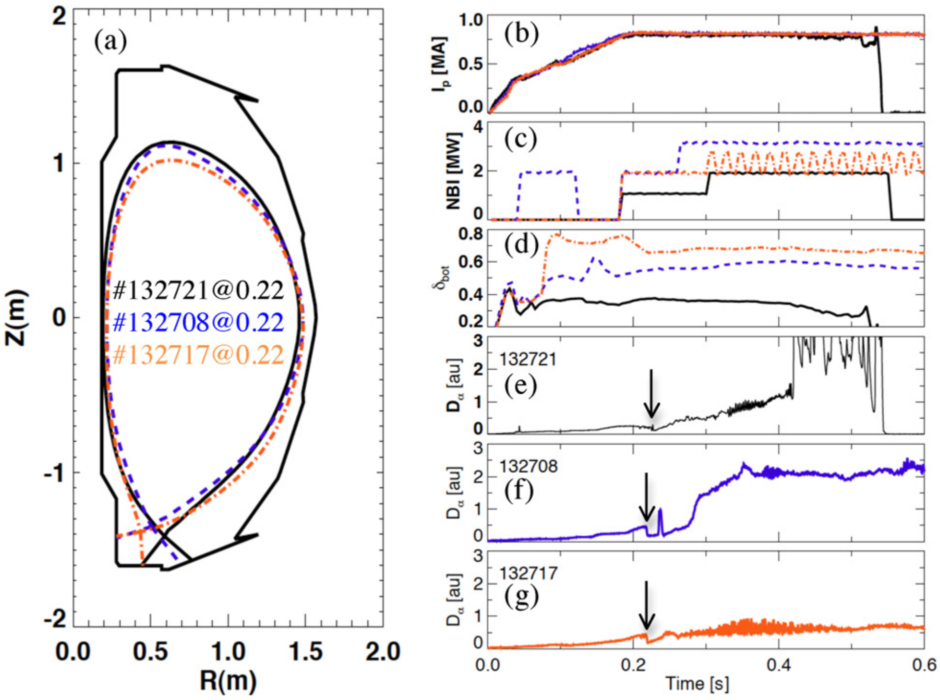

Figure 5. Discharges in δ_{bot} scan: (*a*) three shapes showing low, medium and high δ_{bot} discharges. The temporal evolution of these discharges is shown: (*b*) I_p, (*c*) NBI power, (*d*) δ_{bot}, (*e*)–(*g*) divertor D_α emission for each of the three discharges. The L–H transition times are indicated with arrows.

taken to maintain a constant X-point height, as the measured P_{LH} has been shown to increase with X-point height in various devices [27, 28].

Discharges with three different δ_{bot} values at comparable X-point height were developed, as shown in figure 5(*a*). The other relevant discharge parameters are $I_p = 0.8$ MA, $B_t = 0.45$ T, $\kappa \sim 2$ and X-point height ~ 20 cm. Note that the δ_{bot} variation resulted in a range of $q_{95} \sim 7.5$–9.5 at fixed I_p and B_t. The time evolution of the discharges with P_{heat}^{net} just above P_{LH} is shown in figures 5(*b*)–(*g*). Each of these discharges has a corresponding L-mode discharge with 20–30% less NBI power (not shown). As before, the P_{NBI} was increased in steps through beam voltage variations and pulse-width modulation (figure 5(*c*)). The medium δ_{bot} discharges required additional NBI power during the I_p ramp-up from 40–140 ms to avoid locked modes, but comparisons with and without pre-heating for the low δ_{bot} showed that this level/timing of pre-heating did not affect the timing of the L–H transition or the power threshold. Arrows indicate the time of the L–H transitions on the divertor D_α traces in figures 5(*e*)–(*g*). It can be seen that the lowest δ_{bot} discharge (figure 5(*e*)) required the lowest P_{NBI} of 1.0 MW to trigger the H-mode; both of the higher δ_{bot} discharges (figures 5(*f*), (*g*)) required P_{NBI} of 2.0 MW to trigger the L–H transition.

Figure 6 shows the same measures of input power versus δ_{bot} as discussed above for figures 2 and 4, with the heating powers closest to the P_{LH} indicated with ovals in figure 6(*a*). Because the X-point radius tended to drift with time, the actual value of δ_{bot} at the time of the L–H transition and the corresponding times in the L-mode discharges are plotted, resulting in additional δ_{bot} values than shown in figure 5(*a*). In this case, the trend that the lowest δ_{bot} discharges had 50% lower P_{aux} for an L–H transition power is not reflected in the analysis of P_{loss}. Figure 6(*a*) shows that the required P_{heat}^{net} at the L–H transition is only 33% lower for low δ_{bot} as compared with intermediate and high δ_{bot}. Normalization of P_{heat}^{net} by $\overline{n_e}$ retains the 33% reduction in P_{LH} at the lowest δ_{bot} (figure 6(*b*)). However, inclusion of the P_{OH} and dW_p/dt terms for P_{loss} eliminates the dependence on δ_{bot}, as shown in figures 6(*c*) and (*d*). This is because the lowest δ_{bot} discharges tended to exhibit the highest P_{oh} and the lowest dW_p/dt. Somewhat problematic is the observation that the inclusion of dW_p/dt (and P_{oh} to a smaller extent) into P_{loss} even inverts the ordering of the L-mode and H-mode discharges at medium and high δ_{bot}. In summary, the present analysis indicates that P_{LH} does not depend in a simple manner on δ_{bot}; a more conclusive statement requires clarifying experiments in which the L–H transitions are triggered at times of relatively constant P_{OH} and low dW_p/dt. As a point of reference, we note that nearly all the measured minimum P_{LH} was 4.3–4.7 times the values predicted by the multi-machine scalings discussed in section 1 [5] (the lowest P_{LH} at $\delta = 0.55$ is about 2.5 times the scaling value).

5. Summary and conclusions

We have documented the dependence of the L–H power threshold on a range of parameters in NSTX, focusing partly on the so-called 'hidden variables' not present in international multi-machine scalings. First we note that the P_{LH} increases approximately linearly with $\overline{n_e}$, motivating its use as a normalization parameter. Generally speaking the P_{LH} in NSTX is rather high, i.e. 4–6 times that predicted by the most recent multi-machine scaling [5]. In addition, the $P_{LH}/\overline{n_e}$ is comparable for deuterium and helium discharges. This is not a ubiquitous result in that our measurements agree with

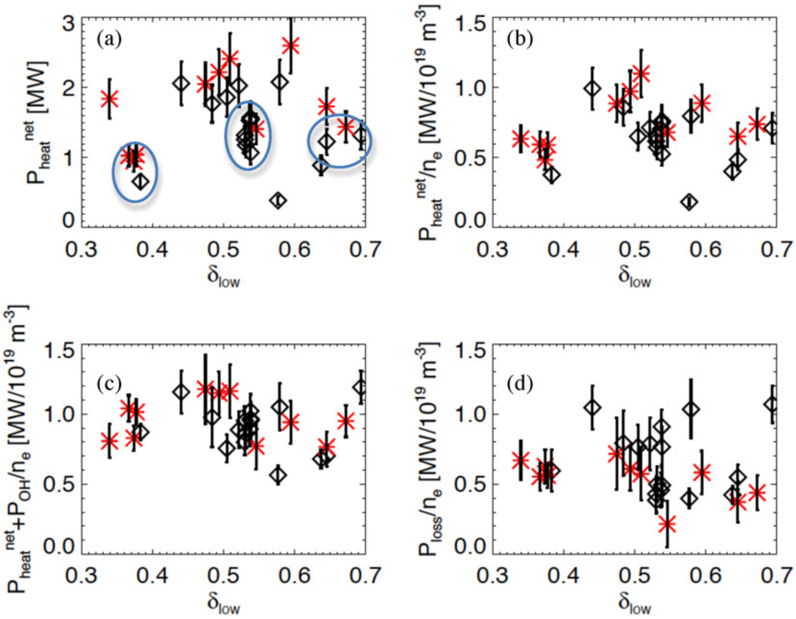

Figure 6. Various metrics of input power as a function of δ_{bot} with NBI heating: (*a*) P_{heat}^{net}, (*b*) P_{heat}^{net} normalized by $\overline{n_e}$, (*c*) (P_{heat}^{net} + P_{oh}) normalized by $\overline{n_e}$ and (*d*) P_{loss} normalized by $\overline{n_e}$. The red stars represent data just prior to an L–H transition and the black diamonds represent data that did not have an L–H transition. Ovals mark discharges closest to the power threshold.

ASDEX-Upgrade results [9], but disagree with results from DIII-D [28] and JET [29], suggesting other parameters are playing a role when comparing deuterium and helium power threshold values. Also, $P_{LH}/\overline{n_e}$ increases strongly with I_p and applied $n = 3$ non-axisymmetric fields and $P_{LH}/\overline{n_e}$ decreases with lithium wall conditioning. The increase in $P_{LH}/\overline{n_e}$ is particularly relevant as ITER is relying on similar fields to suppress ELMs. Our result indicates that the timing of the application will require careful programming so as not to affect the L–H transition timing, which may make it difficult to suppress the first ELM with 100% reliability.

Detailed analysis was presented for the shape dependences of P_{LH}. In particular, shapes very close to a balanced DN with $\delta_r^{sep} \sim 0$ showed a minimum in both the needed P_{aux} and P_{heat}^{net}, as compared with LSN or USN discharges. These differences became less prominent with the inclusion of P_{OH} and $\mathrm{d}W_p/\mathrm{d}t$ to compute P_{loss}. The value of $P_{LH}/\overline{n_e}$ was comparable between NBI and rf heating, despite rather different rotation profiles [19]. Also, the dependence of the required P_{heat}^{net} for H-mode access was clearly a minimum at the lowest δ_{bot}, but these differences were not reflected with the full P_{loss} analysis, mainly because of variations in the P_{OH} and $\mathrm{d}W_p/\mathrm{d}t$. For future machines considering DN operation, it suggests an operational scenario in which a DN configuration can be used to trigger the L–H transition with minimal power, followed by a shape evolution to LSN or USN, if desired for other experiments or scenarios.

While this paper presents the dependences of P_{LH} on normally considered and various 'hidden parameters', as well as the effect of inclusion of various terms in computing P_{loss}, it clearly represents only a first step towards the governing physics. Deeper insight will be obtained through analysis of the edge gradients of dimensional and dimensionless parameters, including particularly E_r and E_r', leading up to the L–H transition [30–33], an activity which is commencing now.

Acknowledgments

This research was supported by the US Department of Energy under contracts DE-AC05-00OR22725, DE-AC02-09CH11466, DE-FC02-04ER54698, DE-FG02-06ER54845, DE-FG03-99ER54519 and DE-FG02-99ER54524. The contributions of the NSTX technical and neutral beam operations are gratefully acknowledged.

References

[1] Wagner F. *et al* 1982 *Phys. Rev. Lett.* **49** 1408
[2] Gormezano C. *et al* 2007 Progress in the ITER Physics Basis, Chapter 6: Steady State Operation *Nucl. Fusion* **47** S285
[3] Lazarus E.A. *et al* 1996 *Phys. Rev. Lett.* **77** 2714
[4] Sabbagh S.A. *et al* 1997 *Proc. 16th Int. Conf. on Fusion Energy 1996 (Montreal, Canada 1996)* vol 1 p 921 (Vienna: IAEA)
[5] Martin Y.R., Takizuka T. and ITPA CDBM H-mode Threshold Database Working Group 2008 *J. Phys.: Conf. Ser.* **123** 012033
[6] Loarte A. 2009 ITER organization, private communication
[7] Ono M. *et al* 2000 *Nucl. Fusion* **40** 557
[8] Bush C.E. *et al* 2006 Spontaneous flows and turbulence in ohmic H-modes in NSTX *Presented at the 11th US-EU TTF Workshop (Marseille, France, 4–7 September 2006)* http://www-fusion-magnetique.cea.fr/ttf2006/prog/drafts/034.pdf
[9] Ryter F. *et al* 2009 *Nucl. Fusion* **49** 062003
[10] Bush C.E. *et al* 2003 *Phys. Plasma* **10** 1755
[11] Sabbagh S.A. *et al* 2006 *Phys. Rev. Lett.* **97** 045004
[12] Menard J.E. *et al* 2007 *Nucl. Fusion* **47** S645
[13] Kugel H.W. *et al* 2008 *Phys. Plasma* **15** 056118
[14] Sabbagh S.A. *et al* 2001 *Nucl. Fusion* **41** 1601
[15] Lao L.L., St John H., Stambaugh R.D., Kellman A.G. and Pfeiffer W. 1985 *Nucl. Fusion* **25** 1611
[16] Meyer H. *et al* 2005 *Plasma Phys. Control. Fusion* **47** 843
[17] Meyer H. *et al* 2006 *Nucl. Fusion* **46** 64
[18] LaBombard B. *et al* 2004 *Nucl. Fusion* **44** 1047
[19] Biewer T.M. *et al* 2006 *Proc. 33rd EPS Conf. on Plasma Physics and Controlled Fusion (Roma, Italy, 19–23 June*

2006) Paper 5.112, http://epsppd.epfl.ch/Roma/pdf/P5_112.pdf

[20] Hawyrluk R.J. *et al* 1980 *Physics of Plasmas Close to Thermonuclear Conditions* vol 1 p 19

[21] Ryan P.M. *et al* 2003 *Proc. 19th Int. Conf. on Fusion Energy (Lyon, France)* paper EX/P2-13

[22] Hosea J.C. *et al* 2008 *Phys. Plasma* **15** 056104

[23] Connor J.W., Hastie R.J., Wilson H.R. and Miller R.L. 1998 *Phys. Plasma* **5** 2687

[24] Wilson H.R., Snyder P.B., Huysmans G.T.A. and Miller R.L. 2002 *Phys. Plasma* **9** 1277

[25] Snyder P.B. *et al* 2002 *Phys. Plasma* **9** 2037

[26] Chang C.S. *et al* 2004 *Phys. Plasma* **11** 2649

[27] Horton L.D. *et al* 2000 *Plasma Phys. Control. Fusion* **42** A37

[28] Gohil P., Jernigan T.C., Osborne T.H., Scoville J.T. and Strait E.J. 2010 *Nucl. Fusion* **50** 064011

[29] Righi E. *et al* 1999 *Nucl. Fusion* **39** 309

[30] Hubbard A.E. *et al* 1998 *Plasma Phys. Control. Fusion* **40** 689

[31] Gohil P., Baylor L.R., Jernigan T.C., Burrell K.H. and Carlstrom T.N. 2001 *Phys. Rev. Lett.* **86** 644

[32] Fielding S.J. *et al* 2001 *Nucl. Fusion* **41** 909

[33] Kaye S.M. *et al* 2003 *Phys. Plasma* **10** 3953